



**EFFECTS OF SOURCE MODELING IN THE FINITE  
ELEMENT METHOD BASED EEG FORWARD PROBLEM**

Masterthesis at the Mathematical Faculty

**Jan Hüwel**

Supervisors:

**Prof. Dr. Carsten Wolters**

**Prof. Dr. Christian Engwer**

February 15, 2021

# Contents

<b>0</b>	<b>Introduction</b>	<b>2</b>
<b>1</b>	<b>Medical Basics</b>	<b>3</b>
<b>2</b>	<b>The Mathematical Theory</b>	<b>4</b>
2.1	The EEG Forward Problem . . . . .	4
2.2	Source Models . . . . .	6
2.3	The CG-FEM Approach . . . . .	7
2.4	Analytical Solution . . . . .	9
<b>3</b>	<b>Method</b>	<b>10</b>
3.1	Patch structure . . . . .	10
3.2	Source construction from dipole patches . . . . .	13
3.3	Experiments . . . . .	15
<b>4</b>	<b>Results</b>	<b>18</b>
4.1	Experiment 1: Modeling error . . . . .	18
4.2	Experiment 2: Numerical error comparison . . . . .	18
4.3	Experiment 3: Quadrupolar approximation . . . . .	22
<b>5</b>	<b>The Multipolar Model</b>	<b>34</b>
5.1	Experiment 4: Optimal Weights . . . . .	35
5.2	The Two-Model Multipole . . . . .	41
<b>6</b>	<b>Conclusion</b>	<b>44</b>
<b>7</b>	<b>Discussion</b>	<b>45</b>
<b>8</b>	<b>Appendix: Using the Code</b>	<b>46</b>
8.1	Using the Source Models in Duneuro . . . . .	46
8.2	Scripts and Datasets . . . . .	46
	<b>Bibliography</b>	<b>49</b>

# Notation

$\Omega$	volume conductor
$\sigma$	conductivity tensor
$j$	current density
$j^p$	primary current density
$j^s$	secondary current density
$u$	electric potential
$u^\infty$	singularity potential
$u^{corr}$	correction potential
$u_{mono}$	electric potential of a monopolar source
$u_{dip}$	electric potential of a dipolar source
$u_{quad}$	electric potential of a quadrupolar source
$\rho$	total electric charge density
$\epsilon_0$	permittivity of free space
$\mu_0$	permeability of free space
$E$	electric field
$B$	magnetic field
$\mathcal{H}^1$	Sobolev space
$x_0$	source position
$M_{mono}$	moment of monopolar source
$M_{dip}$	moment of dipolar source
$M_{quad}$	moment of quadrupolar source

# 0 Introduction

The anatomy and functionality of the human brain is highly complex and has been researched for centuries. Its importance has steadily risen and with modern technology the medical possibilities in this field have improved tremendously. Today, we can analyze a brain's anatomy via imaging techniques like magnetic resonance imaging (MRI) or X-ray computed tomography (CT). We can even monitor its activity with electroencephalography (EEG) or magnetoencephalography (MEG). Combining these methods allows us to localize specific activity in the brain, which is, for example, used in epilepsy diagnosis.

This type of localization via EEG or MEG requires the solution of the corresponding inverse problem, which determines a source's location based on the sensors' signal. The inverse problem is solved numerically and the approaches to solve it build upon the solution for the forward problem, which calculates the sensors' signal for a given source in the brain. Inaccuracies in the forward solution can lead to an inaccurate localization, therefore it is crucial to find the best possible approach to the forward problem.

There has been a lot of research comparing different approaches and this thesis aims to contribute further possibilities. Of the many factors that play into an approach's accuracy, such as the structure of the head model, the amount of layers, the mathematical method and many more, we will specifically look at the possible models to describe the source's structure.

In Chapters 1 and 2 we will introduce the medical and mathematical basics behind the EEG forward problem and the subtraction approach, as well as the possible source models. In Chapter 3 we will describe how we construct patches of activity in the brain and how we will use that to test and compare the source models. Chapter 4 will then present the results of those comparisons. Chapter 5 will introduce another source model, the multipole model, which combines the previously used ones. Lastly we will test this model and devise a conclusion on which model shows the highest accuracy.

The theory in this thesis builds heavily on the work of Leandro Beltrachini[5] and the main focus is to present his methods and our implementation of them into the Duneuro[16, 9, 10] pipeline while also testing their effectiveness compared to the standard model.

# 1 Medical Basics

Most processing of sensory perceptions takes place in the brain, the center of our nervous system. To better understand how we can measure the internal activities of the brain, we will briefly introduce the basic structure and function of its elemental components, the neurons.

A neuron in the brain consists of three main parts: The soma, the dendrites and the axon. The soma is the body of the neuron and the other compartments extend from it. The axon and dendrites build the connection to other cells. Figure 1.1 shows a picture of cortical neurons, where this structure is clearly visible.

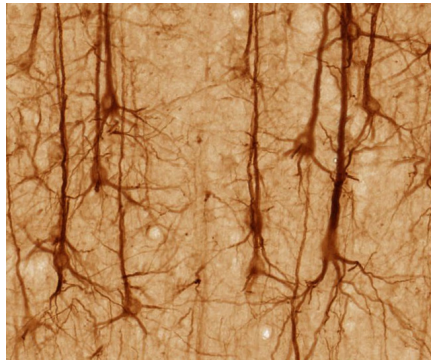


Figure 1.1: Pyramidal neurons in the prefrontal cortex (image from [brainmaps.org](http://brainmaps.org), free to use under creative commons license)

Electrochemical signals can be transmitted from the axon of one neuron to a dendrite of another. With these connections neurons can form complex networks, which in turn are the basis of our nervous system. While each neuron only has one axon, it can build several dendrites, leading to neocortical neurons having 7000 connections on average[7].

The signal transmission starts when a certain threshold for the electric potential in the cell body is reached.  $\text{Na}^+$  ions flow into the cell and raise the membrane potential, whereafter the permeability for  $\text{Na}^+$  drops and the  $\text{K}^+$  permeability increases, lowering the membrane potential back to its resting potential. This process creates an electrical current flowing into the connected dendrites. The resulting increase in potential in all connected neurons causes a dipolar electromagnetic field, which is measurable by electric and magnetic sensors[23].

## 2 The Mathematical Theory

In this chapter we will introduce the EEG forward problem[5, 18, 25], the subtraction approach[18, 25, 8] and multipolar sources[5, 15].

### 2.1 The EEG Forward Problem

The search for the corresponding sensor signal to a given source in EEG and MEG is called the forward problem. Likewise, the localization of a source corresponding to a given signal is called the backward problem or inverse problem[26]. The EEG forward problem[25] stems from the Maxwell equations[15], which are given by

$$\nabla \cdot E = \frac{\rho}{\epsilon_0} \quad (2.1)$$

$$\nabla \times E = -\frac{\partial B}{\partial t} \quad (2.2)$$

$$\nabla \cdot B = 0 \quad (2.3)$$

$$\nabla \times B = \mu_0 \left( j + \epsilon_0 \frac{\partial E}{\partial t} \right), \quad (2.4)$$

with the electric field  $E$ , the total electric charge density  $\rho$ , the permittivity of free space  $\epsilon_0$ , the magnetic field  $B$ , the permeability of free space  $\mu_0$  and the total electric current density  $j$ .

The forward problem is considered quasi-static, so  $\frac{\partial E}{\partial t}$  and  $\frac{\partial B}{\partial t}$  are negligible. Furthermore, the rotation of a vector field is zero if and only if it is conservative. This implies that there is a function  $u$  for the electric potential that satisfies

$$E = -\nabla u.$$

Next we can separate  $j$  into the primary current density  $j^p$  and the secondary current density  $j^s = \sigma E$  where  $\sigma$  describes the conductivity. Combining this with the previous equation yields

$$\begin{aligned} j &= j^p + j^s \\ &= j^p + \sigma E \\ &= j^p - \sigma \nabla u. \end{aligned}$$

Taking the divergence results in

$$\begin{aligned} \nabla \cdot j &= \nabla \cdot j^p - \nabla \cdot (\sigma \nabla u) \\ \Leftrightarrow \nabla \cdot j^p &= \nabla \cdot j + \nabla \cdot (\sigma \nabla u). \end{aligned} \quad (2.5)$$

To reach the final form of the forward problem we go back to the fourth Maxwell equation and recall that our problem is quasi-static and that the divergence of a rotation is always zero.

$$\begin{aligned}
\nabla \times B &= \mu_0 \left( j + \epsilon_0 \frac{\partial E}{\partial t} \right) = \mu_0 j \\
\Leftrightarrow \nabla \cdot \nabla \times B &= \nabla \cdot (\mu_0 j) \\
&\Leftrightarrow 0 = \nabla \cdot (\mu_0 j) \\
&\Leftrightarrow \nabla \cdot j = 0
\end{aligned} \tag{2.6}$$

Inserting (2.6) into (2.5) leads to

$$\nabla \cdot (\sigma \nabla u) = \nabla \cdot j^p. \tag{2.7}$$

Since the electric potential  $u$  is continuous, and the conductivity  $\sigma$  outside of the head domain  $\Omega$  is zero, we get the following Neumann boundary condition[25]:

$$\langle \sigma \nabla u, n \rangle = 0$$

Altogether we have the following Poisson equation as the EEG forward problem:

$$\begin{aligned}
\nabla \cdot \sigma \nabla u &= \nabla \cdot j^p && \text{in } \Omega \\
\sigma \nabla u \cdot n &= 0 && \text{on } \partial\Omega
\end{aligned} \tag{2.8}$$

$\Omega$  is considered open and connected.

In order for a classical solution to this problem to exist,  $\sigma$  needs to be in  $\mathcal{C}^1$ [25]. However, in realistic scenarios we have jumps in the conductivity between different tissues, such as the brain and the CSF. Therefore, we search for weak solutions in the Sobolev space  $\mathcal{H}^1(\Omega)$ .

To transform (2.8) into a weak formulation, we multiply both sides of the main equation with a test function  $\psi$  in a yet to be defined function space  $V$ . Integrating over  $\Omega$  and applying partial integration then gives us

$$a(u, \psi) = \int_{\Omega} \sigma \nabla u \cdot \nabla \psi dx = \int_{\Omega} (\nabla \cdot j^p) \psi dx = l(\psi). \tag{2.9}$$

Our weak solution  $u$  has to solve this equation for all  $\psi \in V$ .

At this point it is difficult to solve this equation, because the term for the primary current density  $j^p$  always has a singularity at the source position  $x_0$ . The exact term depends on the source model and will be introduced later. There are multiple approaches that deal with the singularity in different manners, however this thesis will examine the subtraction approach[25, 8] in particular.

The main idea of this approach is to separate the conductivity  $\sigma$  into the singularity conductivity  $\sigma^\infty$  and the correction conductivity  $\sigma^{corr}$ . We assume that a non-empty subdomain  $\Omega^\infty \subset \Omega$  with homogeneous constant conductivity  $\sigma^\infty$  exists so that the source position lies in  $\Omega^\infty \setminus \partial\Omega^\infty$ . Consequently, the electric potential is also considered

as  $u = u^\infty + u^{corr}$ . The singularity potential  $u^\infty$  is the theoretical solution of (2.8) if  $\Omega$  was an unbounded homogeneous conductor, and it can be calculated analytically. Assuming isotropic homogeneous conductivity  $\sigma^\infty = \bar{\sigma}^\infty I$  lets us rearrange (2.8) into

$$\Delta u^\infty = \frac{\nabla \cdot j^p}{\bar{\sigma}^\infty}. \quad (2.10)$$

This is a simple Poisson equation and thus the solution is well known:

$$u^\infty(x) = -\frac{1}{4\pi\bar{\sigma}^\infty} \int_G \frac{\nabla \cdot j^p(x')}{\|x - x'\|} dx' \quad (2.11)$$

The area  $G \subset \Omega$  needs to be chosen in such a way that it contains the source at  $x_0$  as an interior point.

The exact term for  $\nabla \cdot j^p$  depends on the source model.

## 2.2 Source Models

Before we can determine the term for the primary current density in the different models, we first have to examine the multipolar expansion[21]. For that, let  $\Omega^\infty \subset \Omega$  contain  $y$  and let  $x \in \Omega \setminus \Omega^\infty$  be an arbitrary point. We now want to examine the electric potential  $f(y, x)$  at the point  $x$  caused by a unitary current source at  $y$  and expand it using the Taylor series with expansion point  $x_0$ . We then get

$$f(y, x) = f(x_0, x) + a \cdot \nabla_0 f(x_0, x) + \frac{1}{2} a^T \nabla_0 (\nabla_0 f(x_0, x)) a + \dots$$

with  $a = y - x_0$ . It is proven that this series converges for  $\|a\| < \|x - x_0\|$ [21]. This is given for all  $x \in \Omega \setminus \Omega^\infty$  if the expansion point  $x_0$  is closer to the source location  $y$  than to  $\partial\Omega^\infty$ .

Given this form, we can now calculate the potential in  $x$  due to the entire source  $-\nabla \cdot j^p$ [13]:

$$\begin{aligned} u(x) &= - \int_{\Omega^\infty} f(y, x) \nabla \cdot j^p(y) dy \\ &= - \int_{\Omega^\infty} (\nabla \cdot j^p(y)) f(x_0, x) \\ &\quad + (\nabla \cdot j^p(y)) (y - x_0) \cdot \nabla_0 f(x_0, x) \\ &\quad + (\nabla \cdot j^p(y)) \frac{1}{2} (y - x_0)(y - x_0)^T : \nabla_0 (\nabla_0 f(x_0, x)) \\ &\quad + \dots dy \\ &= M_{mono} f(x_0, x) \\ &\quad + M_{dip} \cdot \nabla_0 f(x_0, x) \\ &\quad + \frac{1}{2} M_{quad} : \nabla_0 \nabla_0 f(x_0, x) \\ &\quad + \dots \end{aligned} \quad (2.12)$$

Here,  $M_{mono}$ ,  $M_{dip}$  and  $M_{quad}$  refer to the monopolar, dipolar and quadrupolar moment respectively and  $:$  is the tensor contraction for the rank-2 tensor  $M_{quad}$ , which satisfies  $(aa^T) : \nabla_0 \nabla_0 f = a^T (\nabla_0 \nabla_0 f) a$ .

If we employ  $\nabla \cdot j^p(x) = -q_{mono} \delta(x - x_0)$  with  $q_{mono} \in \mathbb{R}$ , then it quickly follows that

$$\begin{aligned} M_{mono} &= - \int_{\Omega^\infty} \nabla \cdot j^p(y) dy = q_{mono}, \\ M_{dip} &= - \int_{\Omega^\infty} (\nabla \cdot j^p(y))(y - x_0) dy = 0 \text{ and} \\ M_{quad} &= - \int_{\Omega^\infty} (\nabla \cdot j^p(y))(y - x_0)(y - x_0)^T dy = 0. \end{aligned}$$

In the same manner,  $\nabla \cdot j^p(x) = -q_{dip} \nabla \delta(x - x_0)$  yields

$$\begin{aligned} M_{mono} &= 0 \\ M_{dip} &= q_{dip} \\ M_{quad} &= 0 \end{aligned}$$

for  $q_{dip} \in \mathbb{R}^3$  and  $\nabla \cdot j^p(x) = -\frac{1}{2} q_{quad} : \nabla (\nabla(x - x_0))$  with  $q_{quad} \in \mathbb{R}^{3 \times 3}$  results in

$$\begin{aligned} M_{mono} &= 0 \\ M_{dip} &= 0 \\ M_{quad} &= q_{quad}. \end{aligned}$$

Given these results we now have the terms to insert into (2.11) for purely monopolar, dipolar or quadrupolar sources. The possibility of a multipolar term will be discussed later.

## 2.3 The CG-FEM Approach

With the previous findings we can now determine the analytical solution to (2.10) for monopolar, dipolar and quadrupolar sources. These solutions are[5]:

$$u_{mono}^\infty = \frac{1}{4\pi\bar{\sigma}^\infty} \frac{M_{mono}}{\|x - x_0\|} \quad (2.13)$$

$$u_{dip}^\infty = \frac{1}{4\pi\bar{\sigma}^\infty} \frac{M_{dip} \cdot (x - x_0)}{\|x - x_0\|^3} \quad (2.14)$$

$$\begin{aligned} u_{quad}^\infty &= \frac{1}{4\pi\bar{\sigma}^\infty} \frac{M_{quad}}{2} : \frac{\|x - x_0\| I_3 - 3(x - x_0)(x - x_0)^T}{\|x - x_0\|^5} \\ &= \frac{Tr(M_{quad}) \|x - x_0\| - 3 \sum_{i=1}^3 \sum_{j=1}^3 M_{quad\ i,j} (x - x_0)_i (x - x_0)_j}{8\pi\bar{\sigma}^\infty \|x - x_0\|^5} \end{aligned} \quad (2.15)$$

The respective gradients of  $u^\infty$  will be needed to calculate the correction potential. They are given by

$$\nabla u_{mono}^\infty = -\frac{1}{4\pi\bar{\sigma}^\infty} \frac{M_{mono}(x-x_0)}{\|x-x_0\|^3} \quad (2.16)$$

$$\nabla u_{dip}^\infty = \frac{1}{4\pi\bar{\sigma}^\infty} \left( \frac{M_{dip}}{\|x-x_0\|^3} - \frac{(M_{dip} \cdot (x-x_0))(x-x_0)}{\|x-x_0\|^5} \right) \quad (2.17)$$

$$\begin{aligned} \nabla u_{quad}^\infty = & \frac{1}{8\pi\bar{\sigma}^\infty \|x-x_0\|^5} \left( \frac{-5(x-x_0)}{\|x-x_0\|^2} \left[ Tr(M_{quad}) \|x-x_0\|^2 \right. \right. \\ & \left. \left. - 3\sum_{i=1}^3 \sum_{j=1}^3 M_{quad\ i,j} (x-x_0)_i (x-x_0)_j \right] \right. \\ & \left. + 2Tr(M_{quad})(x-x_0) - 3(M_{quad} + M_{quad}^T)(x-x_0) \right) \quad (2.18) \end{aligned}$$

The next step is to calculate  $u^{corr}$ . For this we can transform (2.8) by inserting the assumptions of the subtraction approach, which results in the following equations:

$$\begin{aligned} -\nabla \cdot (\sigma \nabla u^{corr}) &= \nabla \cdot (\sigma^{corr} \nabla u^\infty) && \text{in } \Omega \\ \sigma \nabla u^{corr} \cdot n &= -\sigma \nabla u^\infty \cdot n && \text{on } \partial\Omega \end{aligned} \quad (2.19)$$

This system can now be solved numerically by using the Finite Element Method. Determining the weak formulation of (2.19) is done in the same way that we used earlier to get (2.9). This leads to the equation

$$\begin{aligned} a(u^{corr}, \psi) &= \int_{\Omega} \sigma \nabla u^{corr} \cdot \nabla \psi dx \\ &= - \int_{\Omega} \sigma^{corr} \nabla u^\infty \cdot \nabla \psi dx - \int_{\partial\Omega} \sigma^\infty \nabla u^\infty \cdot n \psi ds = l(\psi) \end{aligned} \quad (2.20)$$

which needs to be fulfilled for every  $\psi$  in a chosen function space  $V$ . For the CG-FEM [18, 24] approach, this function space consists of Lagrangian ansatz functions.

To further define  $V$  we first need a triangulation  $\mathcal{T}_h$  of  $\bar{\Omega}$ , where  $h \in \mathbb{R}_+$  is the fineness of the triangulation.  $\mathcal{T}_h$  should fulfill the following properties:

- each finite element  $E \in \mathcal{T}_h$  is a closed set and  $\mathring{E}$  is non-empty
- $\bar{\Omega} = \bigcup_{E \in \mathcal{T}_h} E$
- $E_1, E_2 \in \mathcal{T}_h, E_1 \neq E_2 \Rightarrow E_1 \cap E_2 = \emptyset$
- for each  $E \in \mathcal{T}_h$ ,  $\partial E$  is Lipschitz-continuous

Given this triangulation we can construct the function space as follows.

$$V_h = \{v_h \in \mathcal{C}^0(\Omega) : v_h|_E \in \mathcal{P}_1 \forall E \in \mathcal{T}_h\}$$

In this case,  $\mathcal{P}_1$  is the space of all 3-dimensional first degree polynomials. This implies that every function  $v \in V_h$  is uniquely defined by its values at the nodes  $N_i$  of  $\mathcal{T}_h$ , where  $i = 1, \dots, n_h$  and  $n_h$  is the amount of nodes in the triangulation. The set  $\{\varphi_i : i = 1, \dots, n_h\}$  is therefore a basis of  $V_h$  with the basis functions being defined by  $\varphi_i(N_j) = \delta_{i,j} \forall i, j = 1, \dots, n_h$ .

We can now use this basis to describe  $u_h^{corr}$ , which is the closest approximation of  $u^{corr}$  in  $V_h$  since  $u^{corr}$  is not necessarily in this space: Let  $u_i^{corr} = u^{corr}(N_i)$  for all  $i = 1, \dots, n_h$ . Then it follows that  $u_h^{corr} = \sum_{i=1}^{n_h} u_i^{corr} \varphi_i$ .

The bilinear form  $a$  in the weak formulation (2.20) can therefore be rewritten as

$$a(u_h^{corr}, \varphi_i) = \sum_{j=1}^{n_h} u_j^{corr} \int_{\Omega} \sigma \nabla \varphi_j \cdot \nabla \varphi_i dx \quad (2.21)$$

The whole equation can now be considered as a system of linear equations by defining the matrix  $A = (a_{i,j})_{i,j=1,\dots,n_h}$  with

$$a_{i,j} = a(\varphi_i, \varphi_j) = \int_{\Omega} \sigma \nabla \varphi_i \cdot \nabla \varphi_j dx$$

and the vectors  $\mathbf{u}^{corr} = (u_i^{corr})_{i=1,\dots,n_h}$  and  $\mathbf{l} = (l(\varphi_i))_{i=1,\dots,n_h}$ . The system is then given by

$$A \mathbf{u}^{corr} = \mathbf{l}. \quad (2.22)$$

Finding  $\mathbf{u}^{corr}$  solves the EEG forward problem.

## 2.4 Analytical Solution

In a multi-layer spherical head model with layerwise constant conductivity, the equation (2.8) can be solved analytically[14]. In practice, the restriction on the head model prevents this kind of solution from being used, because the caused inaccuracy exceeds the possible numerical inaccuracy in a more realistic head model. However, the analytical solution works great as a point of reference to evaluate the performance of numerical approaches. This is what we use it for in this thesis.

Given such a spherical model with piecewise homogeneous and anisotropic conductivity, the analytical solution to the forward problem at position  $x \in \mathbb{R}^3$  caused by a dipole source at  $x_0 \in \mathbb{R}^3$  is

$$u_{ana}(x_0, x) = \frac{1}{4\pi} M_{dip} \cdot \left[ \frac{x_0}{\|x_0\|} (S_1 - \cos(\omega) S_0) + \frac{x}{\|x\|} S_0 \right] \quad (2.23)$$

with

$$S_0 = \frac{1}{\|x_0\|} \sum_{n=1}^{\infty} (2n+1) R_n(x_0, x) P'_n(\cos(\omega)) \text{ and}$$

$$S_1 = \sum_{n=1}^{\infty} (2n+1) R'_n(x_0, x) P_n(\cos(\omega)),$$

where  $\omega$  is the angle between  $x$  and  $x_0$ ,  $P_n$  is the n-th Legendre polynomial and  $R_n$  is a function that depends on the sphere layers and their conductivities. The exact formula can be found in [14], where this method is explained in detail.

## 3 Method

In order to measure the accuracy and general performance of the models, we will perform a set of experiments. In these experiments we will mainly compare the numerical solution for point-source to the analytical solution for a dipole patch. Our goal is to find the source model that is best suited to approximate a patch of activity. The reason for our point of reference being a dipole patch is that it is a simple yet realistic simulation of real cortical activity. In the brain, any process involves large networks of neurons. The exact range of possible sizes of these networks is difficult to determine, but in this thesis we will use areas from 25 to 625 mm<sup>2</sup>, as these values are comparable to other studies[5, 13]. These areas will all be oriented either radially or tangentially. The precise structure will be described below.

While a point-source is an approximation of realistic activity, it is fast in comparison to the complete modeling of a patch and it is the basis of the mathematical methods that were described in the last chapter.

In order to conduct the experiments we use the Duneuro pipeline[16, 9, 10] via its python (<https://www.python.org>) interface. Duneuro is a C++ toolbox that is built upon the Dune library (<http://dune-project.org>)[1, 2, 3, 4, 6] to allow the solving of the EEG forward problem. The Duneuro code is available on GitLab (<https://gitlab.dune-project.org/duneuro>) and on the Duneuro homepage ([www.duneuro.org](http://www.duneuro.org)). We have added the option of monopolar and quadrupolar sources by allowing Duneuro to transform a given dipole into different types of sources. The exact process will be explained later. This method keeps the simplicity of the system for the user while bringing in the possible benefits of new source models. The analytical solutions that we use as a point of reference are calculated with the software SimBio[20].

The patches and corresponding point-sources will be placed on a tetrahedral mesh of a spherical head model with four compartments, namely the scalp, the skull, the cerebro-spinal fluid (CSF) and the brain. The outside radii of the layers are 92 mm, 86 mm, 80 mm and 78 mm respectively. The mesh has 54771 nodes and the conductivities that were used are 0.00043, 0.00001, 0.00179 and 0.00033.

### 3.1 Patch structure

A simulated patch is constructed from a singular dipole by forming a grid of patch-dipoles around it. This grid is spanned by a normalized vector  $V_1$  that is orthogonal to the original dipole's moment  $M$ , and the cross product  $V_2$  of this vector  $V_1$  with  $M$ . If the original dipole is oriented radially, then all the smaller dipoles will also be radial. This is achieved by creating radial moments from the distance vector between

the sphere's center and the dipole's position, and scaling it accordingly. The same goes for tangential orientation, however the patch-dipoles' moments are just scaled versions of the original moment vector, because they don't need to be reoriented. In the following two theorems we will proof the legitimacy of these structures.

**Definition 3.1 (Construction of radial patches)** *Given a radial dipole  $p_0 = (x_0, m_0)$  with position  $x_0 \in \mathbb{R}^3$  and moment  $m_0 \in \mathbb{R}^3$ , a grid width  $h \in \mathbb{R}$ , the center  $c \in \mathbb{R}^3$  of the head model and the desired amount of patch-dipoles  $N \in \mathbb{N}$  with  $\exists n \in \mathbb{N}_0 : N = (2n + 1)^2$  we define a radial patch around  $p_0$  as follows:*

$$P_{rad} = \{p_{i,j} = (x_{i,j}, m_{i,j}) \in \mathbb{R}^3 \times \mathbb{R}^3 \mid i, j \in [-n, n] \cap \mathbb{Z}, \\ x_{i,j} = x_0 + ihV_1 + jhV_2, \\ m_{i,j} = \frac{s_{i,j}}{N} \frac{x_{i,j} - c}{\|x_{i,j} - c\|}\}$$

where  $V_1$  and  $V_2$  are the orthonormal vectors described earlier and  $s_{i,j}$  is a scaling factor defined by

$$s_{i,j} = \|m_0\| \frac{\|x_{i,j} - c\|}{\|x_0 - c\|}$$

**Theorem 3.1** *A radial patch  $P_{rad}$  constructed from a radial dipole  $p_0$  fulfills:*

1.  $x_0 = \frac{1}{N} \sum_{i=-n}^n \sum_{j=-n}^n x_{i,j}$ ,
2.  $m_0 = \sum_{i=-n}^n \sum_{j=-n}^n m_{i,j}$  and
3.  $m_{i,j}$  is radial for all  $i, j \in [-n, n] \cap \mathbb{Z}$ .

**Proof 3.1**

1.

$$\begin{aligned} \frac{1}{N} \sum_{i=-n}^n \sum_{j=-n}^n x_{i,j} &= \frac{1}{N} \sum_{i=-n}^n \sum_{j=-n}^n x_0 + ihV_1 + jhV_2 \\ &= \frac{1}{N} \sum_{i=-n}^n \sum_{j=-n}^n x_0 \\ &= \frac{N}{N} x_0 \\ &= x_0 \end{aligned}$$

2.

$$\begin{aligned}
& \sum_{i=-n}^n \sum_{j=-n}^n m_{i,j} = \sum_{i=-n}^n \sum_{j=-n}^n \frac{s_{i,j}}{N} \frac{x_{i,j} - c}{\|x_{i,j} - c\|} \\
&= \sum_{i=-n}^n \sum_{j=-n}^n \frac{s_{i,j}}{N} \frac{x_0 + ihV_1 + jhV_2 - c}{\|x_{i,j} - c\|} \\
&= \frac{\|m_0\|}{N} \sum_{i=-n}^n \sum_{j=-n}^n \frac{x_0 + ihV_1 + jhV_2 - c}{\|x_0 - c\|} \\
&= \frac{\|m_0\|}{N} \left( \sum_{i=1}^n \sum_{j=1}^n \frac{(x_0 + ihV_1 + jhV_2 - c) + (x_0 - ihV_1 - jhV_2 - c)}{\|x_0 - c\|} \right. \\
&\quad + \sum_{i=1}^n \sum_{j=1}^n \frac{(x_0 + ihV_1 - jhV_2 - c) + (x_0 - ihV_1 + jhV_2 - c)}{\|x_0 - c\|} \\
&\quad + \sum_{j=1}^n \frac{(x_0 + jhV_2 - c) + (x_0 - jhV_2 - c)}{\|x_0 - c\|} \\
&\quad \left. + \sum_{i=1}^n \frac{(x_0 + ihV_1 - c) + (x_0 - ihV_1 - c)}{\|x_0 - c\|} \right) \\
&\quad + \frac{x_0 - c}{\|x_0 - c\|} \\
&= \frac{\|m_0\|}{N} \left( \sum_{i=1}^n \sum_{j=1}^n \frac{2(x_0 - c)}{\|x_0 - c\|} + \sum_{i=1}^n \sum_{j=1}^n \frac{2(x_0 - c)}{\|x_0 - c\|} \right. \\
&\quad \left. + \sum_{j=1}^n \frac{2(x_0 - c)}{\|x_0 - c\|} + \sum_{i=1}^n \frac{2(x_0 - c)}{\|x_0 - c\|} + \frac{x_0 - c}{\|x_0 - c\|} \right) \\
&= \|m_0\| \frac{4n^2 + 4n + 1}{N} \frac{x_0 - c}{\|x_0 - c\|} \\
&= \|m_0\| \frac{(2n + 1)^2}{N} \frac{x_0 - c}{\|x_0 - c\|} \\
&= \|m_0\| \frac{x_0 - c}{\|x_0 - c\|} \\
&= m_0
\end{aligned}$$

3. This statement is trivial since  $m_{i,j}$  is a scaled version of  $x_{i,j} - c$  and therefore radial.

□

**Definition 3.2 (Construction of tangential patches)** Given a tangential dipole  $p_0 = (x_0, m_0)$  with position  $x_0 \in \mathbb{R}^3$  and moment  $m_0 \in \mathbb{R}^3$ , a grid width  $h \in \mathbb{R}$ , the center  $c \in \mathbb{R}^3$  of the head model and the desired amount of patch-dipoles  $N \in \mathbb{N}$  with  $\exists n \in \mathbb{N}_0 : N = (2n + 1)^2$  we define a tangential patch around  $p_0$  as follows:

$$\begin{aligned}
P_{tan} &= \{p_{i,j} = (x_{i,j}, m_{i,j}) \in \mathbb{R}^3 \times \mathbb{R}^3 \mid i, j \in [-n, n] \cap \mathbb{Z}, \\
&\quad x_{i,j} = x_0 + ihV_1 + jhV_2, \\
&\quad m_{i,j} = \frac{1}{N} m_0\}
\end{aligned}$$

where  $V_1$  and  $V_2$  are again the orthonormal vectors to  $m_0$ .

**Theorem 3.2** *A tangential patch  $P_{tan}$  constructed from a tangential dipole  $p_0$  fulfills:*

1.  $x_0 = \frac{1}{N} \sum_{i=-n}^n \sum_{j=-n}^n x_{i,j}$ ,
2.  $m_0 = \sum_{i=-n}^n \sum_{j=-n}^n m_{i,j}$  and
3.  $m_{i,j}$  is tangential for all  $i, j \in [-n, n] \cap \mathbb{Z}$ .

**Proof 3.2**

1. Identical to the proof of Theorem 3.1
2. Trivial, since  $\sum_{i=-n}^n \sum_{j=-n}^n m_{i,j} = \sum_{i=-n}^n \sum_{j=-n}^n \frac{1}{N} m_0 = m_0$
- 3.

$$\begin{aligned} \langle m_{i,j}, x_{i,j} - c \rangle &= \left\langle \frac{1}{N} m_0, x_0 + ihV_1 + jhV_2 - c \right\rangle \\ &= \frac{1}{N} (\langle m_0, x_0 - c \rangle + ih \langle m_0, V_1 \rangle + jh \langle m_0, V_2 \rangle) \\ &= 0 \end{aligned}$$

In the last step we use the facts that  $p_0$  is tangentially oriented and therefore  $m_0 \perp x_0 - c$  and that  $V_1$  and  $V_2$  were defined to be orthogonal to  $m_0$ .

□

## 3.2 Source construction from dipole patches

Now that we have a way of modeling patches we need to define the corresponding monopolar, dipolar and quadrupolar sources. Our goal is to calculate a source's moment from the patch-dipoles' moments. The sources' position is then set to the center of the patch  $x_0$ .

A single monopolar source is not suitable to approximate a patch of dipoles, because it is impossible to simulate an actual flow of electricity. For the monopolar approximation we therefore use two monopolar sources with a variable distance and equal but opposite strengths. This model resembles the physical dipole which makes the comparison to the mathematical dipole quite interesting. The closer the two monopoles are, the stronger their moments have to be, which is why we will use the following way of constructing them from a patch:

**Definition 3.3 (Monopolar approximation)** *Given a patch  $P$  created from the dipole  $p_0 = (x_0, m_0)$  with  $N \in \mathbb{N}$  dipoles  $(x_1, m_1), \dots, (x_N, m_N) \in \mathbb{R}^3 \times \mathbb{R}^3$  we define*

the monopolar approximation of that patch with distance  $d \in \mathbb{R}$  as a pair of monopoles  $(x_{mono\ 1}, m_{mono\ 1}), (x_{mono\ 2}, m_{mono\ 2}) \in \mathbb{R}^3 \times \mathbb{R}$  with:

$$x_{mono\ 1,2} = x_0 \pm \frac{d}{2\|m_0\|}m_0,$$

$$m_{mono\ 1,2} = \pm \frac{\|m_0\|}{d}.$$

If one wanted to approximate an arbitrary dipole patch that has not necessarily been constructed in the previously defined ways, one could simply define  $x_0$  as the center of the patch and  $m_0$  as the sum of all patch-dipoles' moments and then apply these formulas.

With this approach, the dipolar approximation for an arbitrary patch can be defined as well.

**Definition 3.4 (Dipolar approximation)** *Given a patch  $P$  consisting of  $N \in \mathbb{N}$  dipoles  $(x_1, m_1), \dots, (x_N, m_N) \in \mathbb{R}^3 \times \mathbb{R}^3$ , the dipolar approximation of that patch is the dipole  $(x_{dip}, m_{dip}) \in \mathbb{R}^3 \times \mathbb{R}^3$  with*

$$x_{dip} = \frac{1}{N}\sum_{i=1}^N x_i,$$

$$m_{dip} = \sum_{i=1}^N m_i.$$

Lastly we need a way to construct the parameters of a quadrupolar source from a given dipole patch. There are two approaches to this: The construction can either be based on the dipole approximation of the patch (which is identical to the original dipole if the patch was built around it) or on the patch-dipoles themselves. We will later compare both approaches.

**Definition 3.5 (Quadrupolar approximation 1)** *Given a dipole  $(x_0, m_0) \in \mathbb{R}^3 \times \mathbb{R}^3$ , two vectors  $V_1, V_2 \in \mathbb{R}^3$  with  $m_0 \perp V_1 \perp V_2 \perp m_0$  and  $\|V_1\| = \|V_2\| = \|m_0\|$ , the quadrupole that best approximates the dipole is given by  $(x_{quad}, m_{quad}) \in \mathbb{R}^3 \times \mathbb{R}^{3 \times 3}$  where*

$$x_{quad} = x_0$$

$$m_{quad} = (m_0 \quad V_1 \quad V_2) \begin{pmatrix} 1 & 0 & 0 \\ 0 & 0 & 0 \\ 0 & 0 & 0 \end{pmatrix} (m_0 \quad V_1 \quad V_2)^{-1}$$

The idea behind this approach is to tune the eigenvalues and eigenvectors of the moment matrix to match the given dipole's orientation. This is of course a restrictive use of the quadrupolar model, which is why we try to use more information in the second approach.

**Definition 3.6 (Quadrupolar approximation 2)** Given a patch  $P$  of  $N \in \mathbb{N}$  dipoles  $(x_1, m_1), \dots, (x_N, m_N) \in \mathbb{R}^3 \times \mathbb{R}^3$  we define the quadrupolar approximation of that patch as the quadrupole  $(x_{quad}, m_{quad}) \in \mathbb{R}^3 \times \mathbb{R}^{3 \times 3}$  with

$$x_{quad} = \frac{1}{N} \sum_{i=1}^N x_i$$

$$m_{quad} = \sum_{i=1}^N ((x_i - x_{quad})^T m_i + m_i^T (x_i - x_{quad}))$$

If we would interpret a single dipole as a patch with  $N = 1$ , then the second quadrupolar approximation would have a moment of 0. Therefore this approach is only useful in non-trivial patches. This also makes the comparison between the two approaches non-trivial, however our later experiments will provide the necessary insight in the advantages and disadvantages of each method.

### 3.3 Experiments

Using everything we have defined so far we are now able to conduct the necessary experiments to compare the possibilities of all approaches. We will use common error measures in the field, namely the relative difference measure (RDM) and the  $\ln$  of the magnification factor (lnMAG), in addition to the absolute error.

**Definition 3.7 (Error measures)** Let  $u_1, u_2$  be two solutions to the forward problem. To compare them we define the following error measures:

$$RDM(u_1, u_2) = \left\| \frac{u_1}{\|u_1\|} - \frac{u_2}{\|u_2\|} \right\|$$

$$\ln MAG(u_1, u_2) = \ln \left( \frac{\|u_1\|}{\|u_2\|} \right)$$

$$abs(u_1, u_2) = \|u_1 - u_2\|$$

These measures signify different aspects of the comparison: The lnMAG shows the difference in magnitudes of the solutions, the RDM compares them if they were scaled to the same magnitude and the absolute error combines the two. It is important to keep in mind that the absolute error depends on the magnitude of both solutions, which makes it good comparing  $abs(u_1, u_2)$  with  $abs(u_1, u_3)$ , but unfit for comparing  $abs(u_1, u_2)$  with  $abs(u_3, u_4)$ , given four solutions  $u_1, u_2, u_3, u_4$ .

There are multiple factors that can play into the accuracy of a source model: The difference between the numerical and the analytical solution for a given model, the ability of the chosen model to simulate a realistic source, and factors that can play into these differences, like the depth or orientation of the source. In the upcoming part of the thesis we will look into those factors.

In order to quantify the source properties so that we can analyze their effects, we use purely radial or purely tangential sources and group them by source eccentricity[5].

**Definition 3.8 (Source eccentricity)** *A source at position  $x_0 \in \mathbb{R}^3$  in a spherical head model with center  $c \in \mathbb{R}^3$  and radius of the inner-most layer  $r_{in}$  is  $e \in \mathbb{R}$  with*

$$e = \frac{\|x_0 - c\|}{r_{in}}$$

In our head model the radius  $r_{in}$  is 78 mm.

Before we conduct our own studies we will briefly look into related work by other scholars in this field. One important step to evaluate the accuracy and legitimacy of the different source models is to determine their numerical error, which describes the difference between their numerical solutions and the analytical solutions with the same source model. This has been analyzed by Leandro Beltrachini[5], who found that more complex source models lead to greater numerical errors. This means that the monopolar model has higher numerical accuracy than the dipolar model, while the quadrupolar model is most prone to numerical errors. Using a mesh with a higher resolution also lowers the mismatch between analytical and numerical solutions, meaning that a fine mesh might become a requirement for higher-complexity source models to obtain a very high accuracy. Another factor that raises the error is higher source eccentricity. The numerical approximation for deep sources is better. In order to find results that are easily comparable, we will use only one mesh for our tests, which has been described at the beginning of the chapter.

Our first experiment is the comparison of the two-monopoles approach with the dipole model. The mathematical dipole is an approximation of the physical dipole, but the two-monopoles model resembles the actual physical dipole more closely. The difference in the forward solutions of both models can be used to express how representative the mathematical model of a dipole is of an actual dipolar source. If the difference is considerable, then the usage of a two-monopoles model could improve existing methods of EEG analysis.

The second experiment builds upon the first one and compares the mismatch of the two-monopoles model and an analytical dipole with that of the dipole model and the analytical dipole. It can lead to further insight in the possible applications of the two-monopoles model as factors like source eccentricity and source orientation can affect the models in different ways. To be able to analyze these factors we group the source positions by their eccentricity, and radial and tangential sources are kept separate.

Lastly we will use the introduced formulas for the construction of patches and the approximation via quadrupoles and compare this to the approximation with a single dipole. The sets of sources that we use are comparable to those in the last experiment, but the range of source eccentricities is limited, because the constructed patches should not expand outside the correct layer of the head model or through the center of the sphere. Each dipole in the dataset is used to construct multiple patches of different sizes, from 25 mm<sup>2</sup> to 625 mm<sup>2</sup>. Each patch is approximated as a dipole, a

quadrupole with the method in Definition 3.5, and a quadrupole with the method in Definition 3.6. The numerical solutions for those approximations are then compared to the analytical solution for the patch.

The results of these tests can give us some insight in the effectiveness of the different source models, as well as their performance relative to each other. The Dune and Duneuro code that was used can be found in [10], in the branch 'multipole-subtraction' (at the time of submission). The scripts and datasets for these experiments in particular are submitted with the thesis. All of them are modifications of the scripts and datasets provided by [16]. A small section on how to use the code is included at the end of the thesis.

## 4 Results

In this chapter we discuss the outcome of the previously mentioned experiments and compare our results to previous work on similar topics.

### 4.1 Experiment 1: Modeling error

For the comparison of the two-monopoles model with the dipole model we calculated the forward solution for 500 radial and 500 tangential sources with varying eccentricities. We used multiple variants of the two-monopoles model with different distances between the monopolar sources. These were created as described in Definition 3.3 without the construction of a patch. We then plotted the three error measures for those variants compared to the numerical solution of the dipole model. The results can be seen in Figure 4.1.

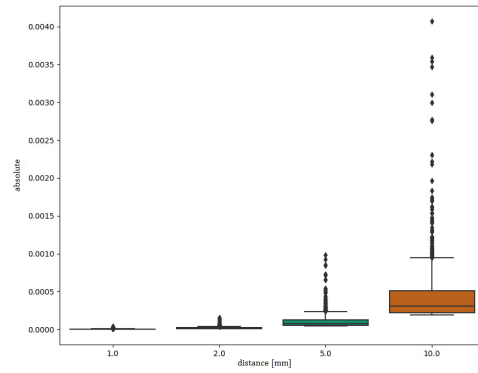
The magnitude of the absolute error is  $10^{-3}$  in the worst case, which shows how close the two approaches are to each other. Of course a smaller distance between the monopoles leads to a smaller error because the mathematical dipole can be seen as the limit of the two-monopoles model when letting the distance go to 0.[15] However, even with a distance as large as 1 *cm* the results are still comparable.

This shows that the mathematical dipole is a very good approximation of the physical dipole.

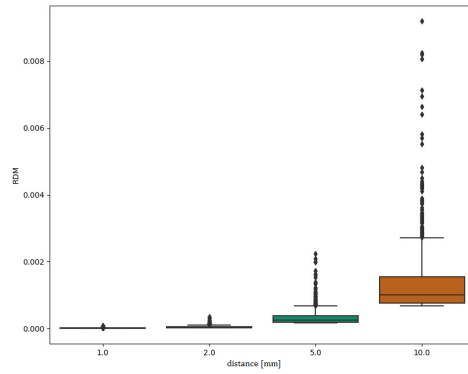
With other methods than the subtraction approach, the results might differ. Schimpf et al[19] examined the same question in a different approach with the result that a greater monopole distance can lead to higher accuracy. This effect is caused by the fact that a larger distance allows more elements of the mesh to be between the monopoles. In the subtraction approach however, this seems to increase the error. Therefore we can not tell from these results alone how well the dipole model approximates a physical dipole in other approaches. This requires further research to be conducted.

### 4.2 Experiment 2: Numerical error comparison

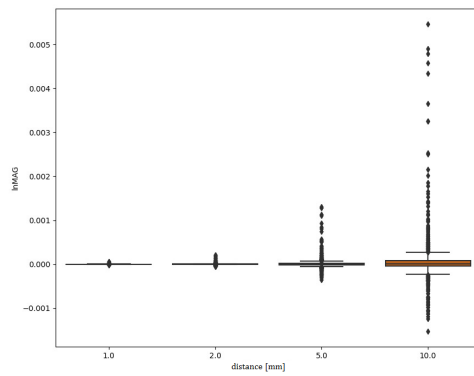
In the second experiment we compare the numerical solutions for the two-monopoles model and the dipole model with the analytical solution of a single dipole. We use a distance of 2 *mm* between the monopoles, which according to the results from the first experiment is different enough from the mathematical dipole to make the results meaningful, while still being small enough to fit in the cortex and therefore be a realistic representation of dipolar activity in the brain. Figure 4.2 shows the results



(a) absolute

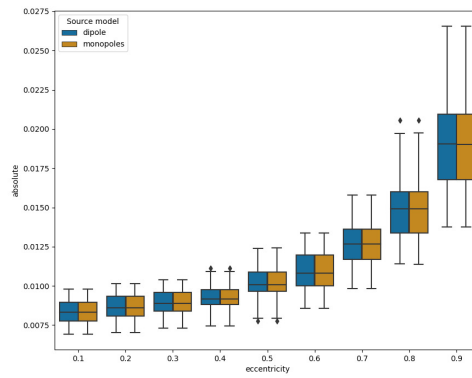


(b) RDM

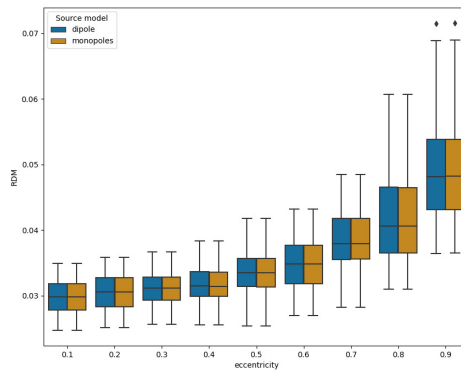


(c) lnMAG

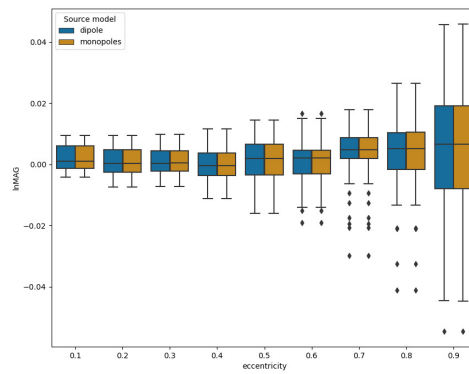
Figure 4.1: Error measures for the difference between the two-monopoles and the dipole model



(a) absolute

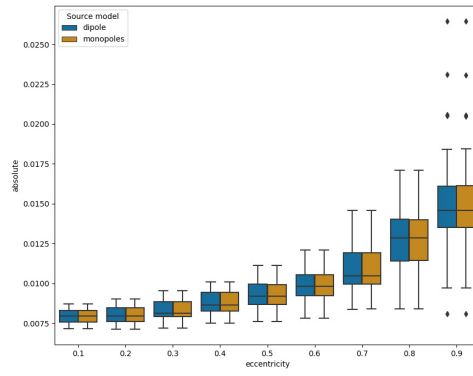


(b) RDM

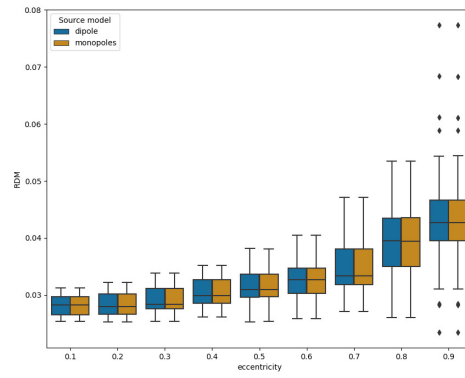


(c) lnMAG

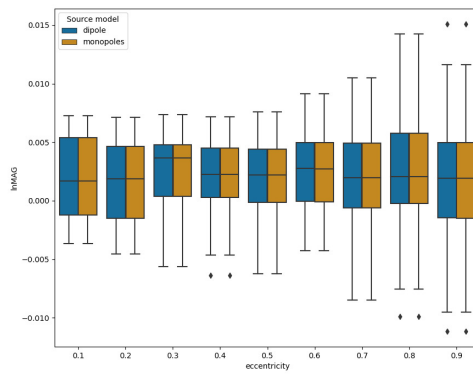
Figure 4.2: Error measures for the two-monopoles model and the dipole model compared to a radial analytical dipole



(a) absolute



(b) RDM



(c) lnMAG

Figure 4.3: Error measures for the two-monopoles model and the dipole model compared to a tangential analytical dipole

for 500 radial sources depending on their eccentricity, and Figure 4.3 does the same for 500 tangential sources.

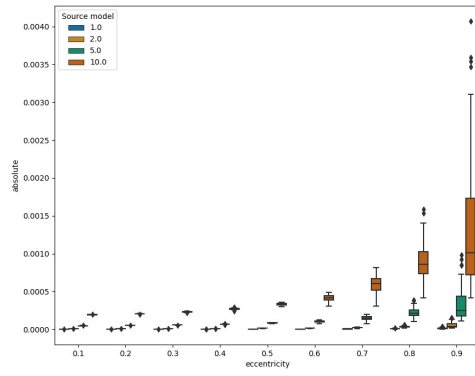
The previously mentioned fact that the numerical error is higher for more eccentric sources can be clearly observed. It is also apparent that tangential sources seem to be better approximated, especially if they are superficial. As for the main focus of this experiment, there seems to be no considerable difference between the two models. The different possible source positions and moments seem to affect both models equally.

To look into this in more detail we repeat experiment 1 with the datasets we used in experiment 2. The results are shown in Figure 4.4 for radial sources and Figure 4.5 for tangential ones. While the absolute error looks similar to the plot in the previous experiment, keep in mind that we are comparing the solution to the numerical dipole instead of the analytical one. This means that the mismatch between the two-monopoles approach and the numerical dipole also increases with a higher source eccentricity and a higher distance between the monopoles. The lnMAG indicates that especially superficial sources tend to have their monopoles-solution be too large in case of radial orientation and too small at tangential orientation. The scaling on the plot also shows clearly that the sources with tangential orientation have a lower RDM between the models than those with radial orientation.

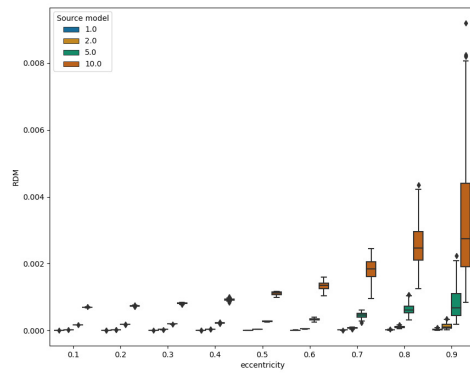
Since the scaling in Figures 4.4 and 4.5 makes it very difficult to see the lnMAG for lower eccentricities, we added these specifically in Figure 4.6. It appears that the lnMAG for tangential sources, most prominently with larger distances between the monopoles, starts above zero for deep sources and then quickly falls below zero for higher eccentricities. An lnMAG of zero indicates that both solutions, in this case the numerical two-monopoles solution and the analytical dipole, have the same magnitude. The fact that the solution for monopoles with a high enough distance is consistently too large for radial and deep tangential sources and too small for superficial tangential sources is something that would benefit from further investigation. However, this topic lies outside of the scope of this thesis and needs to be examined at a later time.

### 4.3 Experiment 3: Quadrupolar approximation

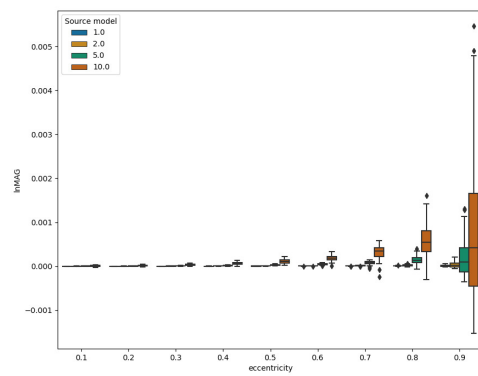
In the last experiment for this chapter we use the methods defined in the previous chapter in order to approximate dipole-patches with quadrupoles. We take one set of 50 radial dipoles and one set of 50 tangential dipoles and construct patches of the sizes  $25 \text{ mm}^2$  to  $625 \text{ mm}^2$  around each source. These patches are then approximated by a point-dipole and by the two types of quadrupoles that were described in the Definitions 3.5 and 3.6. In the plots, the term 'quadrupole' refers to method 1 and 'quadrupole patch' describes method 2. The numerical solutions for all three approximations are then compared to the analytical solution for the patch, which is the sum of all patch-dipoles' analytical solutions. The resulting plots can be seen in Figures 4.7 to 4.10.



(a) absolute

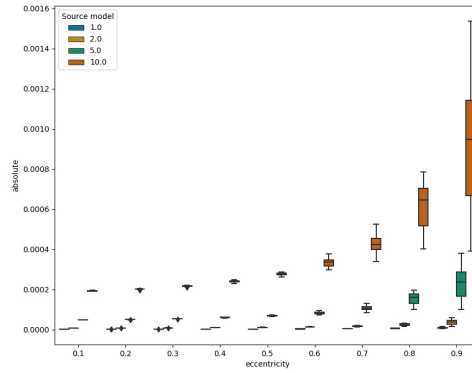


(b) RDM

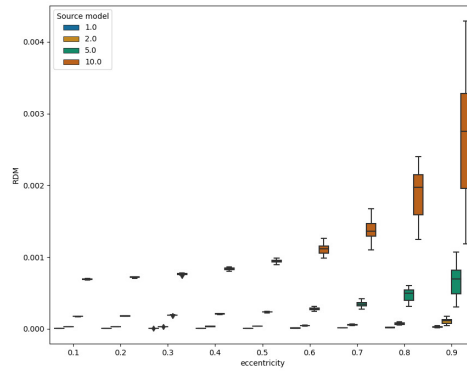


(c) lnMAG

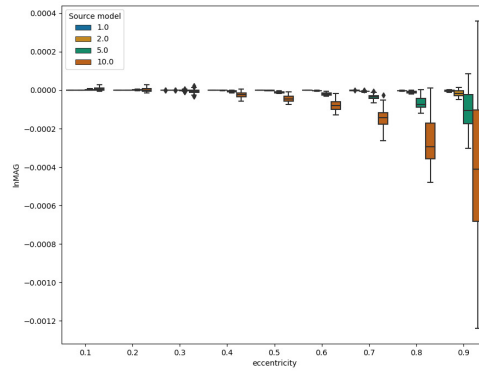
Figure 4.4: Error measures for the difference between the two-monopoles and the dipole model in radial sources



(a) absolute

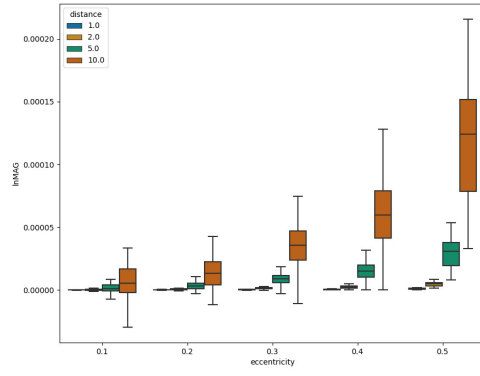


(b) RDM

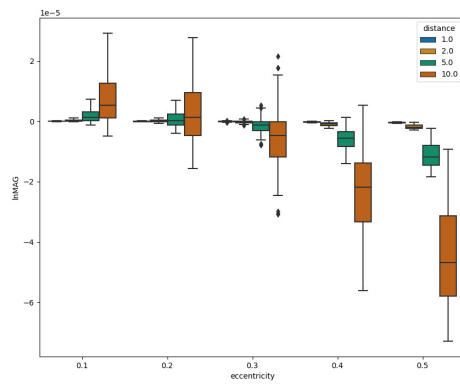


(c) lnMAG

Figure 4.5: Error measures for the difference between the two-monopoles and the dipole model in tangential sources

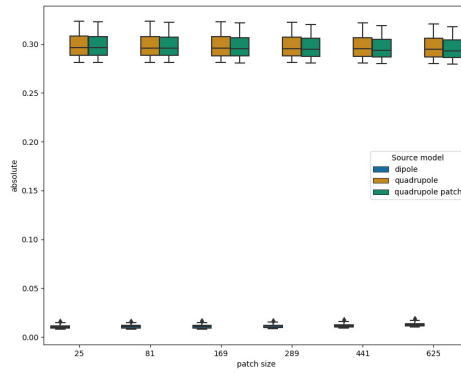


(a) radial

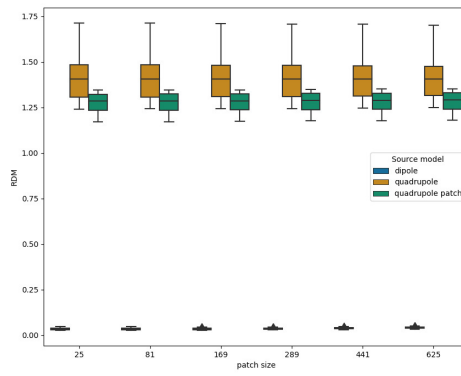


(b) tangential

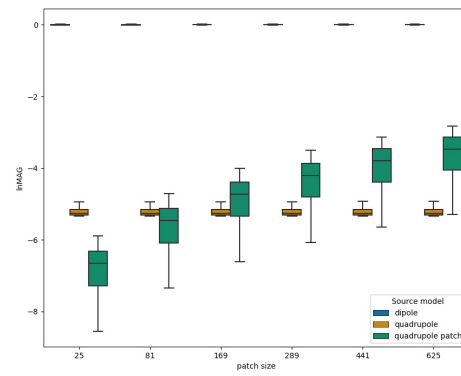
Figure 4.6:  $\ln\text{MAG}$  for sources with low eccentricity between the two-monopoles and the numerical dipole model



(a) absolute

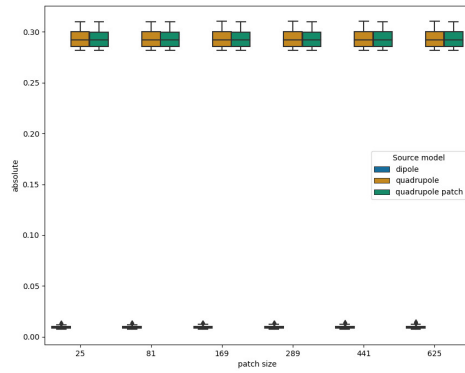


(b) RDM

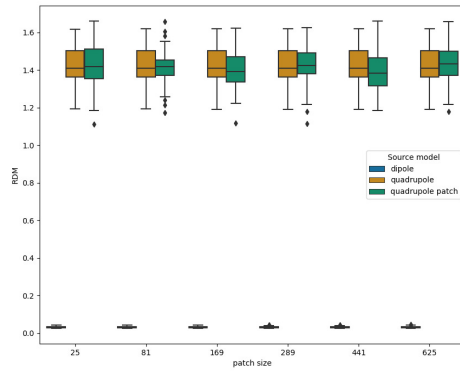


(c) lnMAG

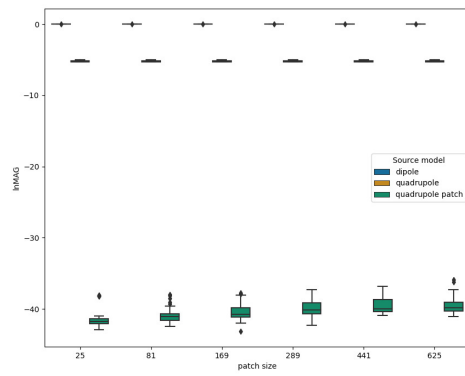
Figure 4.7: Error of the quadrupolar approximation of a radial patch based on patch size



(a) absolute

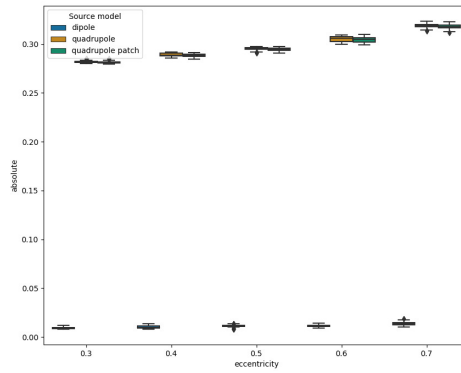


(b) RDM

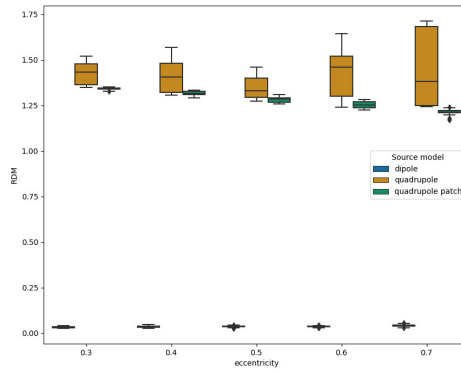


(c) lnMAG

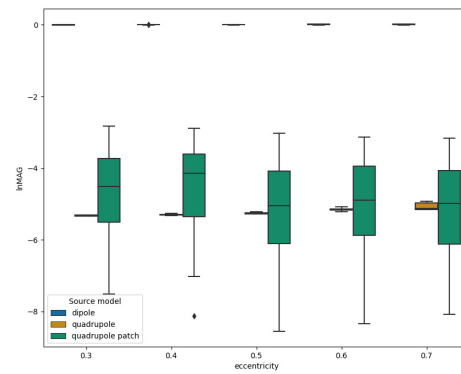
Figure 4.8: Error of the quadrupolar approximation of a tangential patch based on patch size



(a) absolute

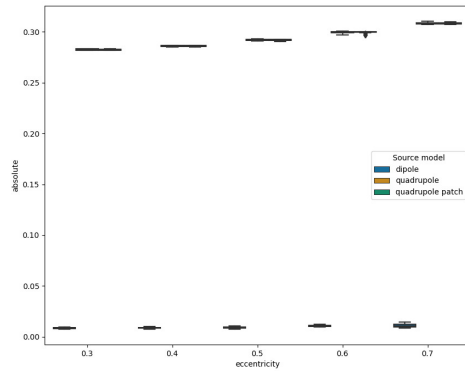


(b) RDM

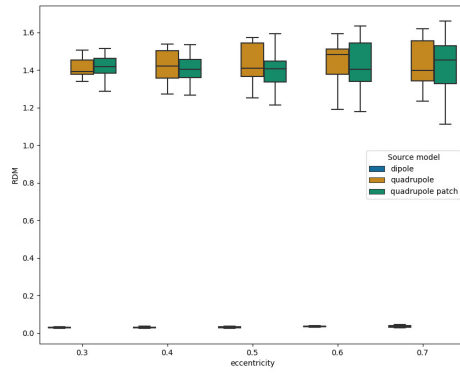


(c) lnMAG

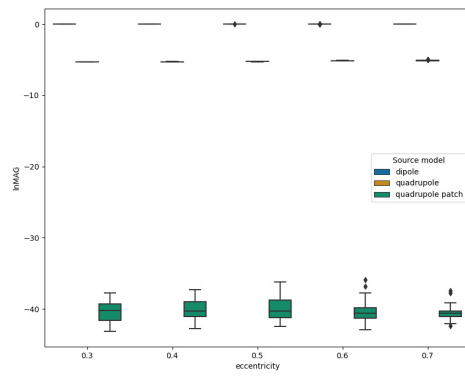
Figure 4.9: Error of the quadrupolar approximation of a radial patch based on eccentricity



(a) absolute



(b) RDM



(c) lnMAG

Figure 4.10: Error of the quadrupolar approximation of a tangential patch based on eccentricity

Looking at the absolute error, it is easy to see that the quadrupolar approximation does not compare well to the dipolar approximation here. The lnMAG clearly shows that the solution for both quadrupolar models is multiple magnitudes smaller than that for the dipole model. In the case of tangential sources, we reveal another problem in our approach through the lnMAG: Using the regular patch structure defined in Definition 3.2 and the approximation in Definition 3.6, the resulting quadrupolar moment is 0, barring computational inaccuracy. In order to get a meaningful quadrupole, we need a less regular patch structure.

The reason for the other quadrupolar approximations also being too small can be seen in the formula for the quadrupole singularity potential in (2.15), as it is one magnitude of  $x - x_0$  smaller than the dipole solution. The monopole solution on the other hand is one magnitude larger, but when we used the two-monopoles approach, this problem was solved. Similarly, if we constructed a physical quadrupole from monopoles, we could approximate it very accurately with our model, but the patch-model that we used seems to resemble a dipole more than a quadrupole. This problem can not be solved by simply scaling the quadrupole solution to the correct magnitude, as the RDM is also worse in comparison to the dipole. A less regular patch structure might lead to different results.

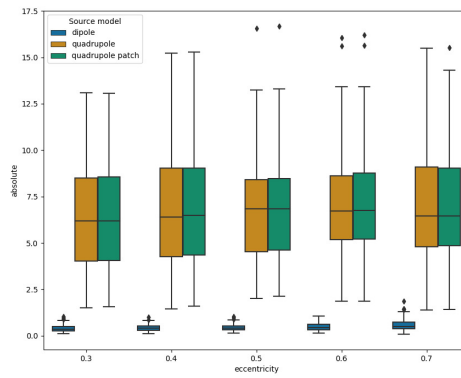
To test this hypothesis, we repeat the experiment with a different way to construct patches: The patch now consists of 625 dipoles that are placed at random in a square with a side-length of 5 *mm* to 25 *mm*. This corresponds to the side-lengths of the patches in the previous iteration of this experiment. The dipole moments are also set at random, but they always have unit length. This means that the patches in this form are no longer radial or tangential, they are an area of irregular activity. While the construction of the area depends on the two spanning vectors, we conducted the experiment in multiple variants and found, that there is no considerable effect of the orientation of those vectors. Therefore we present the results for different possible positions and orientations of these areas together.

The multiple approximations for the activity are calculated as described in Definitions 3.4, 3.5 and 3.6. The dipole that is used as a basis in the quadrupole method 1 is the dipolar approximation of the patch. The resulting comparison is shown in Figures 4.11 and 4.12. While the results seem to be closer to to the desired outcome, the quadrupole still falls behind the dipole approximation in terms of accuracy.

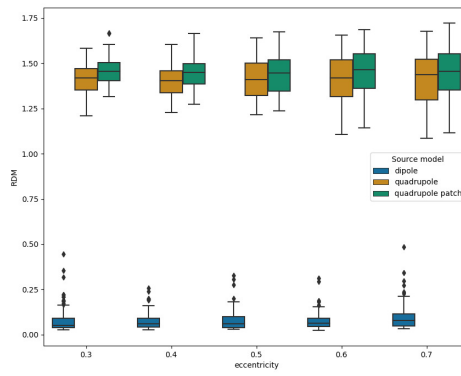
The "quadrupole patch" approach, meaning the approximation with a quadrupole like in method 2, seems to be unaffected by the sources eccentricity. The size of the patch on the other hand is an important factor in the accuracy of the approach, as the lnMAG is closer to zero for larger patches. The absolute error doesn't show this effect, because it is dominated by the patches' solution, while the approximation is far too small in comparison.

Overall, a patch consisting of dipolar sources seems to be best approximated as a dipolar source itself. Since the measurable signal during brain activity may contain a strong dipolar component[17], realistic studies would not benefit from using

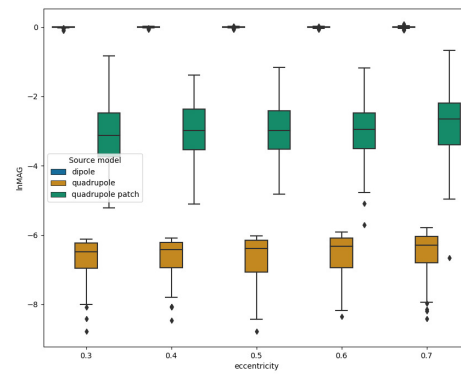
a quadrupolar source model over a dipolar one. However, in the next chapter we will test a different application for the quadrupolar model, to see if it can bring an improvement to the existing methods.



(a) absolute

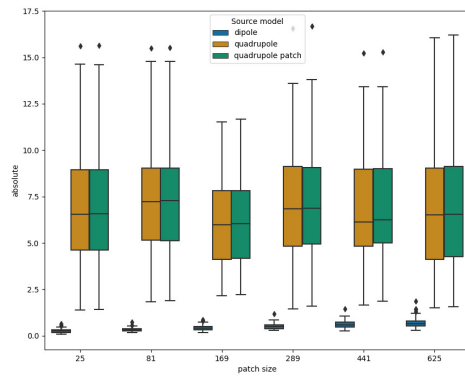


(b) RDM

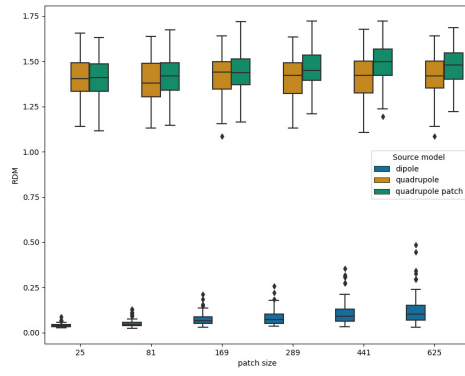


(c) lnMAG

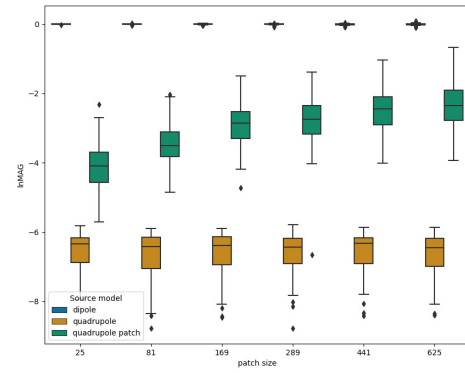
Figure 4.11: Error measures for randomized patch approximation by eccentricity



(a) absolute



(b) RDM



(c) lnMAG

Figure 4.12: Error measures for randomized patch approximation by patch area

## 5 The Multipolar Model

Approximating a dipolar source, either a point-source or a patch, as a quadrupole does not work well. However, it is possible that the dipole model can be improved with additional information. A source model is not limited to one summand in the multipole expansion of a source. So as a last model, we introduce the multipolar source model.

This model combines the previous source models in order to increase the overall performance. As with the quadrupole approximation, there are multiple possible approaches which we will compare. In general, the multipole singularity potential will be calculated as a linear combination of the potentials of the individual source models. Other works on this topic often define the multipolar potential as the direct sum of dipolar and quadrupolar potential[5, 13], but here we want to see if a certain weighting can lead to higher accuracy. It is also possible that including the monopolar model can be beneficial. However, it is reasonable to assume that the two-monopoles approach will not help to increase the accuracy of a multipole, as we showed in the previous chapter that it closely resembles the mathematical dipole.

**Definition 5.1 (Multipolar potential)** *Let  $\Omega \subset \mathbb{R}^3$  be the head domain,  $w_{mono}, w_{dip}, w_{quad} \in \mathbb{R}$  the weights for the linear combination and  $u_{mono}^\infty, u_{dip}^\infty, u_{quad}^\infty : \Omega \rightarrow \mathbb{R}$  the monopolar, dipolar and quadrupolar singularity potential respectively. A multipole is given as  $(x_{mult}, M_{mult})$  where  $x_{mult} \in \mathbb{R}^3$  is the position and  $M_{mult} = (M_{mono}, M_{dip}, M_{quad}) \in \mathbb{R} \times \mathbb{R}^3 \times \mathbb{R}^{3 \times 3}$  is the moment. The multipolar singularity potential  $u_{mult}^\infty : \Omega \rightarrow \mathbb{R}$  is then defined as*

$$u_{mult}^\infty = w_{mono}u_{mono}^\infty + w_{dip}u_{dip}^\infty + w_{quad}u_{quad}^\infty$$

where the individual functions use the source position  $x_{mult}$  and the moment contained in  $M_{mult}$ .

If one wanted to exclude the monopolar aspect from the multipole, one can define  $w_{mono}$  to be zero. Otherwise, the weights still need to be specified.

The quadrupolar moment matrix that is used for the multipole can be determined by either of the two methods we defined in Chapter 3. The results of both models will be compared in the next experiments.

The main point of focus for this source model is the potential increase in accuracy through effective weighting of its components. In order to assess its full potential, we determine the optimal weights by defining the absolute error of the multipole as an error function depending on a vector of weights  $(\omega_1, \omega_2, \omega_3)$ , and employing a minimization algorithm. The resulting optimal parameters are then used to determine all

error measures.

We will conduct multiple experiments with this approach to determine in which situations the model is advantageous. The minimization algorithm that we use is provided by the `scipy.optimize` package[22]. However, the results should be reproducible with all suitable minimization methods.

## 5.1 Experiment 4: Optimal Weights

First we need to test if a multipole model can bring an advantage over the dipole model at all. To do that, we use the dataset of radial sources from experiment 3 and determine optimal weights for each patch size separately. We continue using the regular patch structure, because the irregular patches showed better approximations, therefore the following results will set a lower limit to the usefulness of the multipole approach. The quadrupole moment is determined with method 2, since it proved to be more accurate. The results can be found in Table 5.1.

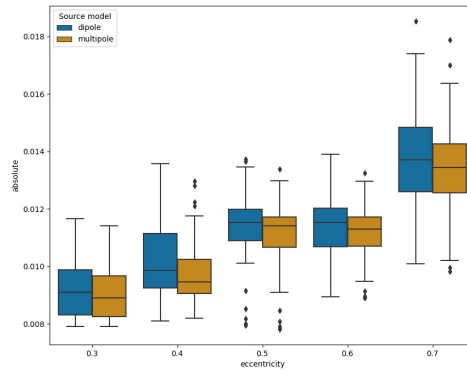
Patch size	$\omega_1$	$\omega_2$	$\omega_3$	Improvement
25 $mm^2$	-1.943e-5	9.988e-1	-1.472e0	0.423%
81 $mm^2$	-1.097e-5	9.980e-1	-6.039e-1	0.686%
169 $mm^2$	2.309e-6	9.968e-1	-4.124e-1	1.236%
289 $mm^2$	2.053e-5	9.952e-1	-3.436e-1	2.197%
441 $mm^2$	4.398e-5	9.932e-1	-3.140e-1	3.618%
625 $mm^2$	7.301e-5	9.906e-1	-3.010e-1	5.407%

Table 5.1: Optimized weights by patch size, method 2

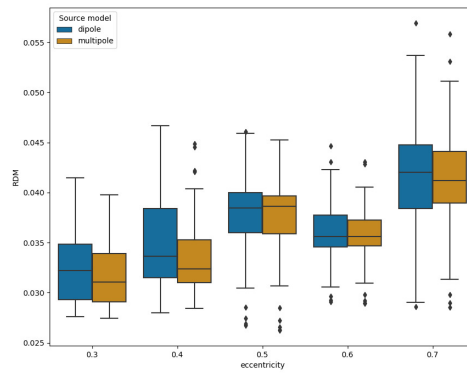
The improvement that is denoted in the table is the decrease in the absolute error, which is also the measure that was optimized over. The comparison of all three measures can be seen in Figure 5.1 and Figure 5.2.

The values in Table 5.1 show a number of interesting relations. While  $\omega_1$  always has a low magnitude, which could stem from the fact that the monopole solution is larger than the dipole one,  $\omega_3$  does not have a large magnitude to balance out the comparably small quadrupole solution. A larger patch size also leads to a smaller contribution of the dipole and the quadrupole and a larger contribution of the monopole, but since the weights for the quadrupole are negative, the decrease of their norm actually increases the quadrupolar component of the multipole. The improvement increases with larger patch size, as the quadrupolar component is more suitable to represent the extent of the area. All these changes are relatively small, but notable.

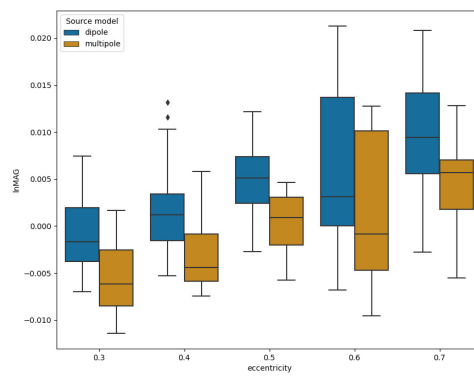
In comparison, the Table 5.2 shows the same data when using quadrupoles constructed with method 1.



(a) absolute

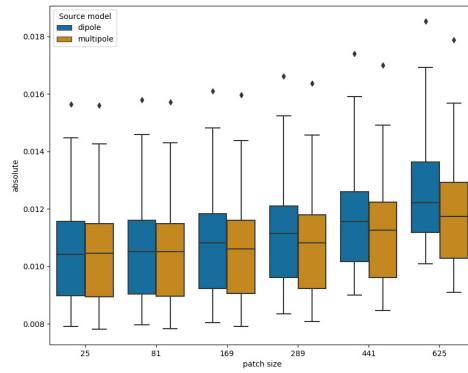


(b) RDM

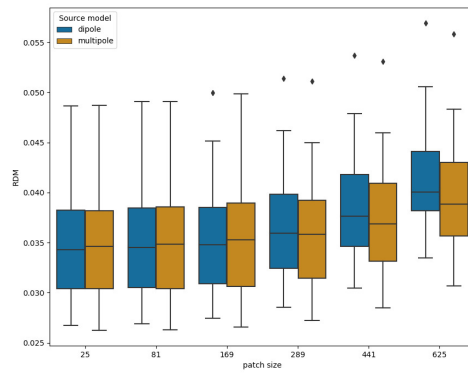


(c) lnMAG

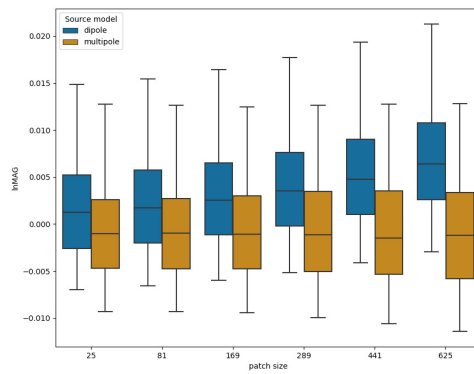
Figure 5.1: Improvement through multipole with method 2 by eccentricity



(a) absolute



(b) RDM



(c) lnMAG

Figure 5.2: Improvement through multipole with method 2 by patch size

Patch size	$\omega_1$	$\omega_2$	$\omega_3$	Improvement
25 $mm^2$	-1.347e-5	9.982e-1	5.643e-2	0.224%
81 $mm^2$	-2.861e-6	9.972e-1	7.182e-2	0.327%
169 $mm^2$	1.393e-5	9.957e-1	9.379e-2	0.545%
289 $mm^2$	3.718e-5	9.936e-1	1.193e-1	0.928%
441 $mm^2$	6.738e-5	9.909e-1	1.447e-1	1.501%
625 $mm^2$	1.050e-4	9.875e-1	1.674e-1	2.228%

Table 5.2: Optimized weights by patch size, method 1

We see very similar effects to the previous test, with the main difference being that the quadrupolar weights are all positive and therefore have increasing norm for larger patches. The improvement is roughly half of the improvement in the previous method. On the other hand, the computational cost for this approach is a lot lower, causing the time required for the quadrupolar component to be roughly 6 times shorter for the smallest patches and over 90 times shorter for the largest ones when compared to the previous approach.

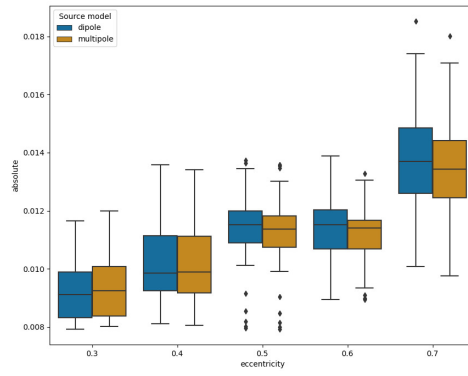
Figures 5.3 and 5.4 show the results for this experiment. It is clearly visible that the improvement in the absolute error stems from a better lnMAG, while the RDM is roughly the same as the one for the dipole approximation. There is a slight improvement in the RDM for large patch sizes, but compared to the previous results, the main focus seems to be on the lnMAG.

Determining the optimal composition of weights requires a reference solution, which we do not have in realistic head models. Therefore it is important to determine general weights that can be applied every time.

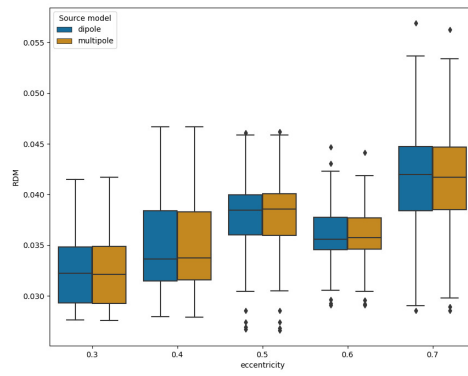
If the patch size is known in advance, then the best approach would be to determine optimal weights in a controlled model, like the spherical head model, and then transfer the results to the realistic application. However, if the patch size needs to be variable, it would work best to optimize weights with an error function that includes a range of possible patch sizes. In our case, this range spans over the patch sizes used in the previous experiments. The results that we got for the optimization are depicted in Table 5.3.

Method	$\omega_1$	$\omega_2$	$\omega_3$	Improvement
Method 1	3.166e-5	9.941e-1	1.047e-1	0.798%
Method 2	1.783e-5	9.955e-1	-3.307e-1	2.235%

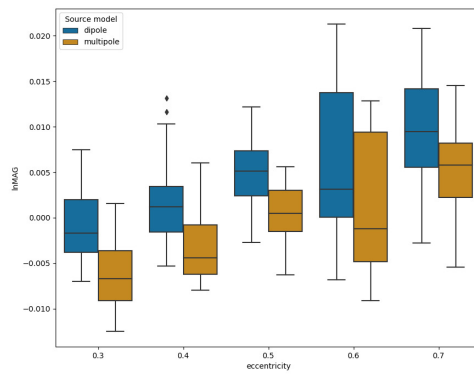
Table 5.3: Optimal weights in our test data for both methods



(a) absolute

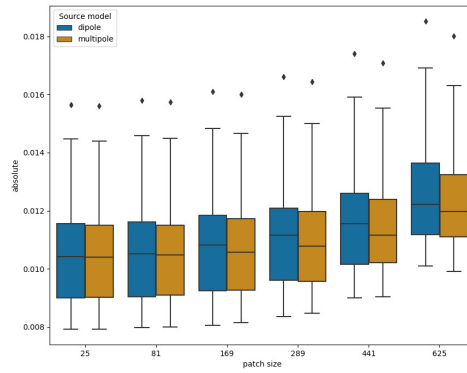


(b) RDM

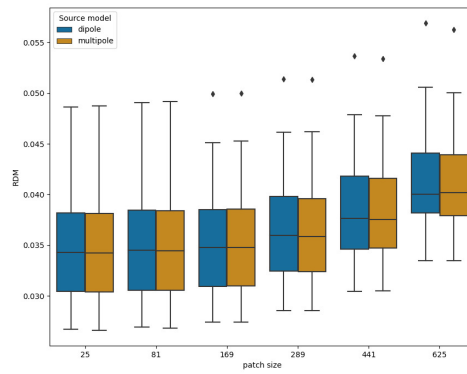


(c) lnMAG

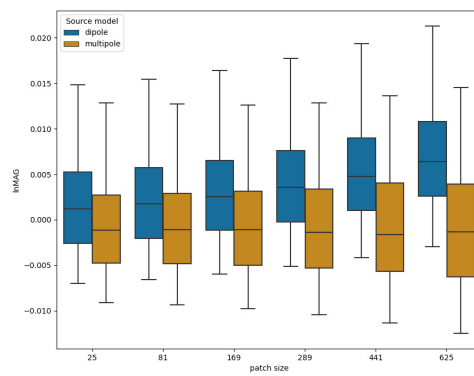
Figure 5.3: Improvement through multipole with method 1 by eccentricity



(a) absolute



(b) RDM



(c) lnMAG

Figure 5.4: Improvement through multipole with method 1 by patch size

The improvement value here is the overall improvement for all patch sizes. Since it is very relevant how this general optimization effects sources of specific sizes, we include these values in Table 5.4.

Method	Patch size	Improvement
Method 1	25 $mm^2$	-0.079%
	81 $mm^2$	0.152%
	169 $mm^2$	0.500%
	289 $mm^2$	0.924%
	441 $mm^2$	1.350%
	625 $mm^2$	1.696%
Method 2	25 $mm^2$	0.154%
	81 $mm^2$	0.524%
	169 $mm^2$	1.184%
	289 $mm^2$	2.194%
	441 $mm^2$	3.542%
	625 $mm^2$	5.110%

Table 5.4: Effects of general optimization by patch size

With this data we can see that the general optimization in method 1 leads to a decrease in accuracy for the smallest patches, and even method 2 only has a very small improvement for that size. The fact that the improvement for large patches with method 2 is still above 5% is very fascinating, because the comparison of the general weights in Table 5.3 and the patch size specific weights in Table 5.1 shows very different values for the monopolar component. This could implicate that the monopole can be left out of the multipole without a big loss of accuracy.

## 5.2 The Two-Model Multipole

The previous results showed that it might be possible to achieve a decent improvement over the dipole model without including the monopole. This would slightly reduce the computational effort and might be worth the consideration in specific situations. To determine the difference in accuracy, we repeat the previous experiments with the restriction, that  $\omega_1$  is always zero. The exact optimal weights are not the focus of this section, therefore we will not present them again. Instead, we present the improvement with the patch size specific optimization in Table 5.5 and the improvement with the general optimization in Table 5.6. We also show the difference in improvement compared to the previous results, given in percentage points.

Method	Patch size	Improvement	Difference
Method 1	25 $mm^2$	0.216%	-0.008
	81 $mm^2$	0.327%	0.000
	169 $mm^2$	0.537%	-0.008
	289 $mm^2$	0.875%	-0.053
	441 $mm^2$	1.343%	-0.158
	625 $mm^2$	1.899%	-0.329
Method 2	25 $mm^2$	0.406%	-0.017
	81 $mm^2$	0.680%	-0.006
	169 $mm^2$	1.235%	-0.001
	289 $mm^2$	2.180%	-0.017
	441 $mm^2$	3.550%	-0.068
	625 $mm^2$	5.249%	-0.158

Table 5.5: Effects of patch size specific optimization

Method	Patch size	Improvement	Difference
Method 1	25 $mm^2$	0.001%	+0.080
	81 $mm^2$	0.203%	+0.051
	169 $mm^2$	0.505%	+0.005
	289 $mm^2$	0.871%	-0.053
	441 $mm^2$	1.237%	-0.113
	625 $mm^2$	1.530%	-0.166
	overall	0.760%	-0.038
Method 2	25 $mm^2$	0.192%	+0.038
	81 $mm^2$	0.551%	+0.027
	169 $mm^2$	1.192%	+0.008
	289 $mm^2$	2.177%	-0.017
	441 $mm^2$	3.498%	-0.044
	625 $mm^2$	5.040%	-0.070
	overall	2.223%	-0.012

Table 5.6: Effects of general optimization

The difference to the previous results shows that the exclusion of the monopolar component leads to a slight overall loss in accuracy, which is more notable in larger patches. The effect of the monopole seems to be stronger when using method 1. This

is confirmed when we take a look back at the optimal weights in the previous section, as the monopolar weights were consistently larger for method 2. On the other hand, we can see an increase in accuracy when using generally optimized weights and applying them to small patches.

We have proven that the multipole model can outperform the classical point-dipole in the approximation of patches. While small patches only offer small possible improvements, the benefits of the multipole model increase with larger patch sizes. Using a higher complexity version by including the monopolar component and determining the exact quadrupolar moment leads to better results overall. However, even a low-complexity version of the multipole model can bring notable advantages.

## 6 Conclusion

In this thesis, we analyzed the effects of different source models in the CG-FEM subtraction approach on the solution of the EEG forward problem. To do that, we introduced the necessary medical and mathematical basics and the physical meaning of the different source models. Afterwards, we conducted multiple experiments to compare the performance of different models using the Duneuro software pipeline[9, 10]. The results showed, that out of the simple source models, the dipole model is best suited to approximate a dipolar patch of sources, which is a realistic representation of cortical activity[17]. The combination of multiple models into a multipole model manages to increase the accuracy slightly at the cost of computation time. Here, a precise calculation of the quadrupole moment works better than the simpler alternative, leading to a possible improvement of up to 5% for the cost of a much longer computation.

The optimal usage of the multipole model depends a lot on the requirements in terms of time and accuracy. The simple model can provide a middle way, raising the accuracy up to 3% for roughly triple the computational effort. Excluding the monopolar component makes the model less dependent on prior knowledge about the area of activity, at the cost of accuracy when that knowledge exists.

The question which source model is optimal can not be answered generally. Every model brings advantages and disadvantages that need to be considered. However, the multipole model is the most adaptable model and can always be fitted to a given problem. It is a viable alternative to the classical dipole model and should be considered in possible future studies.

## 7 Discussion

The results in the first experiments of this thesis are a very good validation of the dipolar source model in the subtraction approach. It is very close to the physical dipole and did not lead to major errors in any of our experiments. If additional accuracy is needed and computational costs is not an important issue, the multipolar source model can provide a powerful alternative. These results have been in line with similar research[5, 13], but it is not necessarily clear if they can be extrapolated to other approaches as well. This would require further investigation.

It is also possible that different source properties, such as eccentricity and orientation, require different weights to be approximated optimally. This question would also benefit from tests with different patch models, and leaves a lot of room to be explored.

In our experiments in Chapter 4, we found an interesting behavior of the physical dipole, simulated as two opposing monopoles with a set distance between them, compared to the mathematical dipole. The difference seems to be smaller in tangential sources, where the solution for the physical dipole is slightly too large in deep sources and gets comparably smaller with higher eccentricity. In radial sources, the solution for the physical dipole exhibits the opposite effect, but the difference in lower eccentricities is not as prominent as in the tangential sources. This relation could reveal an interesting behavior of the mathematical dipole model and requires further research as well.

With the ever increasing computational power that is available and the development of more efficient numerical methods, the disadvantage of longer calculations for the multipole model will disappear gradually. Prior optimization of weights in a controlled model could also become a non-factor eventually. At that point, further research on this topic could be one of the major ways to improve existing methods. Hopefully, this thesis can be a small step towards those improvements.

## 8 Appendix: Using the Code

The different source models that were compared throughout this thesis have all been made available in Duneuro[9, 10]. In this chapter, we will briefly explain how to use them and how to work with the included scripts and datasets.

### 8.1 Using the Source Models in Duneuro

How to start using the Duneuro pipeline is best described in the paper about it by Andreas Nüßing, Maria Carla Piastra, Sophie Schrader, Tuuli Miinalainen, Sampsa Pursiainen, Heinrich Brinck, Carsten H. Wolters and Christian Engwer[16]. Here, we will not go into the general application of the pipeline.

The different source models, namely the single monopole, the two-monopoles model, the dipole, the quadrupole constructed from method 1, the quadrupole constructed from method 2 and the multipole, are only available in the subtraction approach. There is an additional quadrupole option that allows the user to directly enter a moment matrix that is then used for all dipoles. To use these options, the source model configuration, given as a Python dictionary or a Matlab struct array, needs to contain an element called *'expansion'*, which defines which option to use. Depending on the desired source model, additional options can be given. The list of expansions and additional options is given in Table 8.1.

Some important notes: The *'patch size'* option refers to the  $n$  in our patch definitions, meaning that the patch will have  $(2 \cdot \text{'patch size'} + 1)^2$  dipoles on a grid with *'patch shift'* distance between them. The value *'single'* for *'quadrupole mode'* refers to method 1. If nothing is set for *'expansion'*, the forward problem will be solved for a dipolar source.

### 8.2 Scripts and Datasets

There will be 5 different scripts and multiple datasets submitted together with this thesis. We will briefly explain where they were used exactly.

In all experiments, we used the mesh in the file *sphere\_tet\_mesh\_4c.msh* with the conductivities in *sphere\_4c.cond* and the electrode positions in *sphere\_electrodes.txt*. This data has been provided by [16], together with example scripts and dipoles, that have been modified for our experiments.

Source model	Expansion	Additional options (type)	Default values
single monopole	'monopole'	/	/
two-monopoles	'monopoles'	'distance' (double)	2.0
dipole	'dipole'	/	/
quadrupole method 1	'quadrupole'	/	/
quadrupole method 2	'quadrupole patch'	'mode' ('radial'/'tangential')	'radial'
		'patch size' (int)	1
		'patch shift' (double)	1.0
quadrupole	'quadrupole 2'	'M11' (double)	0
		'M12' (double)	0
		'M13' (double)	0
		'M21' (double)	0
		'M22' (double)	0
		'M23' (double)	0
		'M31' (double)	0
		'M32' (double)	0
		'M33' (double)	0
multipole	'multipole'	'weight monopole' (double)	0
		'weight dipole' (double)	1
		'weight quadrupole' (double)	0
		'quadrupole mode' ('single'/'radial'/'tangential')	'single'
		'patch size' (int)	1
		'patch shift' (double)	1.0

Table 8.1: Optional parameters in the source model configuration

The first experiment, where we compared the numerical solutions for the two-monopoles model with that of the dipole model, was executed with the *script\_1.py* script. The set of sources is provided in *dipoles\_1.txt*.

The second experiment, the comparison of numerical monopoles and a numerical dipole with an analytical dipole, used *script\_2.py* with the sources being *dipoles\_2\_r.txt* for radial and *dipoles\_2\_t.txt* for tangential orientation. We then repeated experiment 1 with those sources as well. In the code's comments, this is referred to as 'experiment 1-2'. The restriction on low-eccentricity sources was achieved by applying the first script to the datasets in *dipoles\_1-3\_r.txt* and *dipoles\_1-3\_t.txt*, for radial and tangential sources respectively.

Experiment 3 is given by *script\_3.py* with sources *dipoles\_3\_r.txt* and *dipoles\_3\_t.txt*, while the randomized patches are constructed and analyzed with *script\_3-2.py* and the corresponding dataset *dipoles\_3-2.txt*.

Lastly, experiment 4, where we found optimal weights for the multipole, uses *script\_4.py* with the data from *dipoles\_3\_r.txt*. All experiments in Chapter 5 were conducted with this script, and the different versions can be included or excluded from the code using comments.

All these scripts use the python packages Numpy[11] and Matplotlib[12] and require Python 3.6 or above.

## Bibliography

- [1] P. Bastian, M. Blatt, A. Dedner, N.-A. Dreier, C. Engwer, R. Fritze, C. Gräser, C. Grüniger, D. Kempf, R. Klöfkorn, M. Ohlberger, O. Sander. The DUNE framework: Basic concepts and recent developments. *Computers & Mathematics with Applications* 81, pp. 75-112, 2021
- [2] P. Bastian, M. Blatt, A. Dedner, C. Engwer, R. Klöfkorn, M. Ohlberger, O. Sander. A Generic Grid Interface for Parallel and Adaptive Scientific Computing. Part I: Abstract Framework. *Computing*, 82(2-3), pp. 103-119, 2008
- [3] P. Bastian, M. Blatt, A. Dedner, C. Engwer, R. Klöfkorn, R. Kornhuber, M. Ohlberger, O. Sander. A Generic Grid Interface for Parallel and Adaptive Scientific Computing. Part II: Implementation and Tests in DUNE. *Computing*, 82(2-3), pp. 121-138, 2008
- [4] P. Bastian, M. Blatt. On the Generic Parallelisation of Iterative Solvers for the Finite Element Method. *Int. J. Computational Science and Engineering*,4(1):56-69, 2008
- [5] Leandro Beltrachini. A Finite Element Solution of the Forward Problem in EEG for Multipolar Sources. *IEEE Transactions on Neural Systems and Rehabilitation Engineering* Vol 27 No 3, 2019
- [6] M. Blatt, P. Bastian. The Iterative Solver Template Library. *B. Kåström, E. Elmroth, J. Dongarra and J. Wasniewski. Applied Parallel Computing. State of the Art in Scientific Computing* Volume 4699 of Lecture Notes Scientific Computing, pages 666-675. *Springer*, 2007
- [7] David A. Drachman. Do we have brain to spare?. *Neurology* 64, Jun 2005
- [8] F. Drechsler, C. H. Wolters, T. Dierkes, H. Si and L. Grasedyck. A full subtraction approach for the finite element method based source analysis using constrained Delaunay tetrahedralisation. *NeuroImage* 46(4), pp. 1055-1065, 2009
- [9] Christian Engwer, Jakob Ludewig, Tuuli Miinalainen, Sophia Müller, Andreas Nüßing, Maria Carla Piastra, Sophie Schrader. Duneuro.org (online). Accessed on 08. Jan 2021 at <http://duneuro.org>
- [10] Christian Engwer, Jakob Ludewig, Tuuli Miinalainen, Sophia Müller, Andreas Nüßing, Maria Carla Piastra, Sophie Schrader. Duneuro GitLab (online). Accessed on 08. Jan 2021 at <https://gitlab.dune-project.org/duneuro/duneuro/>

- [11] Charles R. Harris, K. Jarrod Millman, Stéfan J. van der Walt, Ralf Gommers, Pauli Virtanen, David Cournapeau, Eric Wieser, Julian Taylor, Sebastian Berg, Nathaniel J. Smith, Robert Kern, Matti Picus, Stephan Hoyer, Marten H. van Kerkwijk, Matthew Brett, Allan Haldane, Jaime Fernández del Río, Mark Wiebe, Pearu Peterson, Pierre Gérard-Marchant, Kevin Sheppard, Tyler Reddy, Warren Weckesser, Hameer Abbasi, Christoph Gohlke, Travis E. Oliphant. Array programming with NumPy. *Nature*, 585, 357–362, 2020
- [12] John D. Hunter. Matplotlib: A 2D Graphics Environment. *Computing in Science & Engineering*, 9, 90-95, 2007
- [13] K. Jerbi, J. C. Mosher, S. Baillet, R. M. Leahy. Localization of realistic cortical activity in MEG using current multipoles. *NeuroImage* 22, 2004
- [14] J. C. de Munck, Maria J. Peters. A Fast Method to Compute the Potential in the Multisphere Mode. *IEEE Transactions on Biomedical Engineering* Vol 40 No 11, 1993
- [15] Wolfgang Nolting. Grundkurs Theoretische Physik 3 - Elektrodynamik. *Springer*, 10th edition, 2013
- [16] Sophie Schrader, Andreas Westhoff, Maria Carla Piastra, Tuuli Miinalainen, Sampsa Pursiainen, Johannes Vorwerk, Heinrich Brinck, Carsten H. Wolters, Christian Engwer. DUNEuro – A software toolbox for forward modeling in bioelectromagnetism. *arXiv e-prints* arXiv:1901.02874v4, 2021 (submitted)
- [17] Yoshio Okada. Empirical Bases for Constraints in Current-Imaging Algorithms. *Brain Topography*, Vol 5 No 4, 1993
- [18] Maria Carla Piastra. New finite element methods for solving the MEG and the combined MEG/EEG forward problem. Dissertation at *Westfälische Wilhelms-Universität Münster*, 2019
- [19] P. H. Schimpf, Ceon Ramon, Jens Haueisen. Dipole Models for the EEG and MEG. *IEEE Transactions on Biomedical Engineering* Vol 49 No 5, May 2002
- [20] SimBio Development Group. SimBio: A generic environment for bio-numerical simulations (online). Accessed on 12. Feb 2021 at <https://www.mrt.uni-jena.de/simbio>
- [21] J. A. Stratton. Electromagnetic Theory. *McGraw-Hill*, New York, NY, USA, 1941
- [22] Pauli Virtanen, Ralf Gommers, Travis E. Oliphant, Matt Haberland, Tyler Reddy, David Cournapeau, Evgeni Burovski, Pearu Peterson, Warren Weckesser, Jonathan Bright, Stéfan J. van der Walt, Matthew Brett, Joshua Wilson, K. Jarrod Millman, Nikolay Mayorov, Andrew R. J. Nelson, Eric Jones, Robert Kern, Eric Larson, CJ Carey, İlhan Polat, Yu Feng, Eric W. Moore,

- Jake VanderPlas, Denis Laxalde, Josef Perktold, Robert Cimrman, Ian Henriksen, E.A. Quintero, Charles R Harris, Anne M. Archibald, Antônio H. Ribeiro, Fabian Pedregosa, Paul van Mulbregt, and SciPy 1.0 Contributors. SciPy 1.0: Fundamental Algorithms for Scientific Computing in Python. *Nature Methods*, 17(3), 261-272, 2020
- [23] Johannes Vorwerk. Comparison of Numerical Approaches to the EEG Forward Problem. Dissertation at *Westfälische Wilhelms-Universität Münster*, 2011
- [24] J. Vorwerk, J.-H. Cho, S. Rampp, H. Hamer, T. R. Knösche and C. H. Wolters. A Guideline for Head Volume Conductor Modeling in EEG and MEG. *NeuroImage*, 100, pp.590-607, 2014
- [25] Carsten H. Wolters, Harald Köstler, Christian Möller, Jochen Härdtlein, Lars Grasedyck, Wolfgang Hackbusch. Numerical Mathematics of the Subtraction Method for the Modeling of a Current Dipole in EEG Source Reconstruction Using Finite Element Head Models. *SIAM Journal of Scientific Computing* 30(1):24-45, 2007
- [26] C. H. Wolters, L. Grasedyck and W. Hackbusch. Efficient computation of the lead field bases and influence matrix for the FEM-based EEG and MEG inverse problem. *Inverse Prob.*, 20(4):1099, 2004

## Eigenständigkeitserklärung

Hiermit versichere ich, dass die vorliegende Arbeit über Effects of source modeling in the finite element method based EEG forward problem selbstständig von mir und ohne fremde Hilfe verfasst worden ist, dass keine anderen Quellen und Hilfsmittel als die angegebenen benutzt worden sind und dass die Stellen der Arbeit, die anderen Werken – auch elektronischen Medien – dem Wortlaut oder Sinn nach entnommen wurden, auf jeden Fall unter Angabe der Quelle als Entlehnung kenntlich gemacht worden sind. Mir ist bekannt, dass es sich bei einem Plagiat um eine Täuschung handelt, die gemäß der Prüfungsordnung sanktioniert werden kann.

Ich erkläre mich mit einem Abgleich der Arbeit mit anderen Texten zwecks Auffindung von Übereinstimmungen sowie mit einer zu diesem Zweck vorzunehmenden Speicherung der Arbeit in einer Datenbank einverstanden.

Ich versichere, dass ich die vorliegende Arbeit oder Teile daraus nicht anderweitig als Prüfungsarbeit eingereicht habe.

15.02.2021 J Hübl

(Datum, Unterschrift)